Geophysical Journal International

Geophys. J. Int. (2018) **215,** 314–324
Advance Access publication 2018 July 17
GJI Geomagnetism, rock magnetism and palaeomagnetism

doi: 10.1093/gji/ggy285

Energy barriers in three-dimensional micromagnetic models and the physics of thermoviscous magnetization

Karl Fabian[1,2] and Valera P. Shcherbakov[3,4]

[1]*Geological Survey of Norway, Trondheim 7491, Norway. E-mail: Karl.Fabian@NGU.NO*
[2]*CAGE - Centre for Arctic Gas Hydrate, Environment and Climate, University of Tromsø, Tromso 9037, Norway.*
[3]*Geophysical Observatory 'Borok', Borok, Yaroslavskaya Oblast 151742, Russia.*
[4]*Institute of Geology and Petroleum Technologies, Kazan Federal University, Kazan 420008, Russia.*

Accepted 2018 July 16. Received 2018 July 11; in original form 2018 April 3

SUMMARY

A first-principle micromagnetic and statistical calculation of viscous remanent magnetization (VRM) in an ensemble of cubic magnetite pseudo-single domain (PSD) particles is presented. The theoretical methods developed apply to all magnetic particle sizes, from single domain to multidomain. The numerical implementation is based on a fast relaxation algorithm for finding optimal transition paths between micromagnetic local energy minima. The algorithm combines a nudged-elastic-band technique with action minimization. Initial paths are obtained by repetitive minimizations of modified energy functions. For a cubic PSD particle, 60 different local energy minima are identified, and all optimal energy barriers between them are numerically calculated for the case of zero external field. These results are used to estimate the energy barriers in weak external fields. Based on these, time-dependent transition matrices are constructed, which fully describe the continuous homogeneous Markov processes of VRM acquisition and decay. By spherical averaging, the acquisition of remanent magnetization in an isotropic PSD ensemble is calculated from laboratory to geological timescales. The modelled particle ensemble shows a physically meaningful overshooting of magnetization during VRM acquisition. The results also clarify why VRM acquisition in PSD particles can occur much faster than VRM decay, and therefore explain occurrence of extremely stable VRM as found in some palaeomagnetic studies.

Key words: Rock and mineral magnetism; Numerical modelling; Magnetic properties.

1 INTRODUCTION

1.1 Aim and outline of the paper

The geomagnetic field has been recorded by remanent magnetization in newly formed rocks throughout the Earth's history. Therefore, crustal rocks form a palaeomagnetic archive which is accessible through rock magnetic measurements. The interpretation of these measurements requires a thorough understanding of the physical processes by which remanence is acquired. Thermoviscous magnetization of natural pseudo-single domain (PSD) or multidomain particles is the most abundant remanence in palaeomagnetism, although more reliable single domain (SD) remanence carriers are preferred, and theoretical interpretation is based on paradigms developed from SD theory. The main aim of this paper is to describe more advanced computational and conceptional methods to obtain a physical understanding of the remanence acquisition in multidomain particles. The second section introduces a technique to determine energy barriers in micromagnetic models of inhomogeneously magnetized particles that is currently implemented in MERRILL (Ó Conbhuí *et al.* 2018) , and has recently been used in studying magnetizations of rocks and meteorites (Einsle *et al.* 2016; Nagy *et al.* 2017; Shah *et al.* 2018; Valdez-Grijalva *et al.* 2018). Although technically challenging, it is an essential pre-requisite for a quantitative study of thermoviscous magnetization. In the third section, we use the computational method to calculate all energy barriers for a simplified 3-D model of metastable flower and vortex states in a cubic magnetite particle. The fourth section introduces the theoretical background for a statistical analysis of viscous remanence acquisition and decay in weak fields, based on Markov processes across the computed energy barriers between the metastable states. This links the micromagnetic energy barrier calculation to statistical analytic techniques as employed in (Fabian 2003; Newell 2006). In the fifth section, this theory is applied to the energy barriers calculated in Section 3, and the physical meaning of the model results obtained is discussed.

1.2 Micromagnetic modelling

Micromagnetic modelling is now a standard technique to determine stable and metastable magnetization states in small ferro- and ferrimagnetic particles. It is used to calculate and analyse magnetization structures in natural and synthetic magnetic nanoparticles. This size range is of special interest in rock magnetism where the reconstruction of the Earth magnetic field depends critically on the reliability of remanence carriers in natural rocks. The grain size distribution of these remanence carriers rarely is confined to the relatively small SD-sized range. Accordingly, detailed knowledge of the physical mechanism of magnetization change in larger nanoparticles is needed to assess and evaluate the magnetic measurement results from natural materials. Because of its importance for understanding remanence acquisition in natural rocks, rock magnetic studies were among the first to apply numerical micromagnetic models. The first approach to estimate barriers between SD and two-domain states used a 1-D model of magnetization change (Enkin & Dunlop 1988). When 3-D models were developed to understand inhomogeneous remanence states (Williams & Dunlop 1989) , it was immediately a main interest to obtain energy barriers to model the acquisition of thermoremanence (Enkin & Williams 1994; Thomson *et al.* 1994; Winklhofer *et al.* 1997; Muxworthy *et al.* 2003). Knowing the energy barriers between different magnetization states within a single particle also leads to a quantitative prediction of magnetic viscosity and magnetic stability of remanence information, even over geological timescales. An important result of early micromagnetic calculations was that beyond the regime where exchange forces dominate, that is, beyond length scales of several exchange lengths $\sqrt{A/K_d}$, there exist a multitude of local energy minima (LEM) corresponding to metastable magnetization structures (Williams & Dunlop 1989; Fabian *et al.* 1996; Rave *et al.* 1998). In the context of thermoviscous remanence, the most important property of metastable magnetization structures m is their residence time $\tau(m)$. It denotes the expectation value of the time during which the system remains in state m, if it initially is in this state at time $t = 0$. The residence time $\tau(m)$ directly depends on the transition probabilities $p(m, m')$ between m and all other LEM m', which in turn depend upon the possible transition pathways. To determine the transition probability $p(m, m')$ in very good approximation, it is sufficient to find the most likely transition path between m and m', which is the path with the lowest energy barrier. This path runs across the saddle point with lowest energy of all which connect m and m'. Therefore, the problem of finding the transition probabilities $p(m, m')$ is closely related to finding saddle points in high-dimensional micromagnetic energy landscapes.

1.3 Statistical theory

Given these transition probabilities, the geologically important mechanism of thermoremanence acquisition can be described as a stochastic process of magnetization change in a temperature-dependent energy landscape. Its transition matrix is related to $p(m, m')$, determined by the energy barriers between the possible states (Fabian 2003).

2 ACTION AND PATH INTEGRALS

2.1 Micromagnetic modelling

Berkov (1998a,b,c) developed a numerical method to evaluate the distribution of energy barriers between metastable states in many-particle systems. It determines the optimal path between the two given metastable states by minimizing the thermodynamic action in the Onsager–Machlup functional (Onsager & Machlup 1953) for the transition probability. The macroscopic variables in this approach are magnetizations of individual volume elements which are exposed to statistically independent thermal fluctuations. The thermodynamic action is then derived from a Langevin equation of motion for the individual magnetizations under the influence of independent Gaussian thermal fluctuations (Berkov 1998c). In the limit of low temperature, this method essentially performs a local saddle-point search in a high-dimensional energy landscape. Mathematically, similar problems exist in several disciplines of physics and chemistry. Several methods to locate saddle points have been developed in these fields (Henkelman & Jónsson 2000a; Henkelman *et al.* 2000b; Olsen *et al.* 2004) and an improved nudged-elastic band (NEB) technique for micromagnetics was presented by Dittrich *et al.* (2002). The fundamental difficulty in energy-barrier computation is that micromagnetic structures m for interesting realistic particle sizes have to be described by many variables and that their energy E is a highly nonlinear function of m. Already minimizing $E(m)$ requires sophisticated algorithms, but for energy-barrier calculations it is even necessary to determine saddle points in this high-dimensional energy landscape.

Several approaches are available for this task, but because saddle-point calculation is equivalent to minimizing $\|\nabla E(m)\|^2$, all rapidly converging methods require second derivatives of E. This, however, is rather to be avoided if the calculation should be performed effectively.

This study develops a combination of several of the above cited techniques to efficiently calculate energy barriers in micromagnetic models.

2.2 Action minimization

Berkov (1998a) introduced action minimization as a tool for finding optimal transition paths in thermally driven micromagnetic systems. He discretized the time-dependent action of the magnetic particle system and used a numerical quadrature representation for direct numerical minimization. This rigorous approach is complicated by its explicit dependence upon transition time. However, transition paths turn out to be geodesics of the energy surface in the limit of infinite transition time, where energy barriers are lowest.

Dittrich *et al.* (2002) make use of this fact by directly searching for geodesic paths using a modification of the NEB algorithm of Henkelman & Jónsson (2000a) and Henkelman *et al.* (2000b).

A problem of this algorithm is that it involves the numerical solution of a large system of ordinary differential equations. Moreover, there is a tendency of the NEB algorithm to produce spurious up-down-up movements along the gradient (kinks) which cannot be completely removed in all cases.

Here, we combine both approaches by designing a path relaxation algorithm similar to NEB, but constrained to decrease the action at each step. The algorithm performs a fast gradient-like relaxation from an initial path towards the optimal transition path. It detects and avoids the development of kinks and does not involve numerical solutions of differential equations.

The important problem of finding an initial path which is likely to lie in the basin of attraction of the optimal transition path under the proposed relaxation scheme is also investigated.

2.3 Geometric action

Here we define the *geometric action* for a path p as the minimal thermodynamic action for any transition along this path. This means that for a given shape of the path, we find the optimal velocity that minimizes the action along this path. In a general mechanic system, with unit-free vector x of degrees of freedom, the action of a transition process $x(t)$ from state $x(0) = x_0$ into $x(t_{\mathrm{end}}) = x_1$ is defined by

$$S(x(t)) := \int_0^{t_{\mathrm{end}}} \langle \dot{x} + \nabla E, \dot{x} + \nabla E \rangle \, \mathrm{d}t. \tag{1}$$

Here $\langle v, w \rangle$ denotes the scalar product of the vectors v and w, $\dot{x}$ is the time derivative of the vector $x(t)$ of independent parameters and ∇E is the derivative of the energy functional E with respect to these parameters. In our application, E will be the normalized micromagnetic energy as a function of the magnetization structure. A general derivation of this explicit form of thermodynamic action can be found in Graham (1975) eqs (2.18) and (2.20). The probability that the specific transition process $x(t)$ occurs depends monotonically on $\exp(-S(x(t)))$. In the next section, we will be looking for the optimal transition path in the energy landscape determined by E. The quality of any given geometric path p is defined as its geometric action: the action of the one transition process $x_p(t)$, among all possible transition processes $x(t)$ moving along p, which minimizes eq. (1).

We start with a canonical parametrization of p by arc length s (see e.g. Do Carmo 2016) and try to find a reparametrization $s(t)$ which minimizes S along p. For this optimal transition process we then have

$$S_{\min}(p) = S(x_p(t)) = \int_0^{L(p)} \langle \frac{\mathrm{d}x}{\mathrm{d}s} v + \nabla E, \frac{\mathrm{d}x}{\mathrm{d}s} v + \nabla E \rangle \frac{\mathrm{d}s}{v}, \tag{2}$$

where $L(p)$ is the arc length and $v(s) = \frac{\mathrm{d}s}{\mathrm{d}t}(s)$ is the local velocity of the optimal transition at arc length s. Finding $s(t)$, thus is reduced to the variational problem of finding the function $v(s)$ which minimizes eq. (2). The corresponding Euler–Lagrange equation is

$$\frac{\mathrm{d}}{\mathrm{d}v}\left(\frac{1}{v}\langle \frac{\mathrm{d}x}{\mathrm{d}s} v + \nabla E, \frac{\mathrm{d}x}{\mathrm{d}s} v + \nabla E \rangle\right) = 0. \tag{3}$$

A short calculation confirms that its solution is

$$v = \|\dot{x}\| = \|\nabla E\| \left\| \frac{\mathrm{d}x}{\mathrm{d}s} \right\|^{-1} = \|\nabla E\|, \tag{4}$$

where the norm is defined by $\|v\|^2 = \langle v, v \rangle$. The last equality in eq. (4) uses the fact that for the arc-length parametrization $\|\mathrm{d}x/\mathrm{d}s\| = 1$. Inserting this result into eq. (2) yields

$$\begin{aligned} S_{\min}(p) &= 2 \int_0^{L(p)} \|\nabla E\| \left\| \frac{\mathrm{d}x}{\mathrm{d}s} \right\| + \left\langle \frac{\mathrm{d}x}{\mathrm{d}s}, \nabla E \right\rangle \mathrm{d}s \\ &= 2 \int_0^{L(p)} \|\nabla E\| + \left\langle \frac{\mathrm{d}x}{\mathrm{d}s}, \nabla E \right\rangle \mathrm{d}s. \end{aligned} \tag{5}$$

This integral can be simplified further by noting that

$$\begin{aligned} &\int_0^{L(p)} \left\langle \frac{\mathrm{d}x}{\mathrm{d}s}, \nabla E \right\rangle \mathrm{d}s = \int_{E(x_0)}^{E(x_1)} \mathrm{d}E \\ &= E(x_1) - E(x_0) =: \Delta E. \end{aligned} \tag{6}$$

Accordingly, one obtains the geometric action of p as

$$S_{\min}(p) = 2\,\Delta E + 2 \int_0^{L(p)} \|\nabla E\| \, \mathrm{d}s. \tag{7}$$

Because the geometric action only depends on the shape of the curve p connecting the endpoints x_0 and x_1, for finding the optimal transition path one can now directly calculate the variation of $S_{\min}(p)$ with respect to geometric changes of the path, and need not consider changes in velocity along the same path anymore.

2.4 Finding the optimal path by variation of the geometric action

It is possible to find the Euler–Lagrange equations for the optimal path by variation of the geometric action $S_{\min}(p)$ with respect to x.

To this end we reparametrize eq. (7) by $w(s) = s/L(p)$ and obtain

$$S_{\min}(p) = 2\,\Delta E + 2 \int_0^1 \|\nabla E\| \left\| \frac{\mathrm{d}x}{\mathrm{d}w} \right\| \mathrm{d}w. \tag{8}$$

The Euler–Lagrange equation of the variational problem $\delta S_{\min}(p) = 0$ after some simplification assumes the form

$$\frac{\mathrm{d}^2 x}{\mathrm{d}s^2} = \nabla \log \|\nabla E\|. \tag{9}$$

The details of the calculation are given in the Appendix.

2.5 The least-action path follows steepest energy descent

In the 1-D case, eq. (4) directly implies that the optimal transition path fulfils the condition

$$\dot{x} = \pm \nabla E. \tag{10}$$

This is also true in the multidimensional case where it not simply follows from eq. (4) but requires an additional argument: based on the Cauchy inequality applied to eq. (8), the following inequality is valid for the optimal path p:

$$S_{\min}(p) \geq 2\,\Delta E + 2 \int_0^1 \left| \left\langle \nabla E, \frac{\mathrm{d}x}{\mathrm{d}w} \right\rangle \right| \mathrm{d}w. \tag{11}$$

By dividing the integration interval [0,1] into finitely many intervals $[w_k, w_{k+1}]$ with alternating constant sign of $\langle \nabla E, \mathrm{d}x/\mathrm{d}w \rangle$ one can perform the integration over each of these intervals and obtains

$$S_{\min}(p) \geq 2\,\Delta E + 2 \sum_{k=0}^{K} |\, E(x(w_{k+1})) - E(x(w_k))| \,. \tag{12}$$

Because the right-hand side is a lower limit of $S_{\min}$, a path which fulfils eq. (10) achieves equality in eq. (11) and therefore coincides with the least-action path between the prescribed endpoints.

Equality in eq. (12) means that the least action depends only upon the energies at the points w_k. Because the sign of $\langle \nabla E, \mathrm{d}x/\mathrm{d}w \rangle$ changes at w_k, but the speed $\mathrm{d}x/\mathrm{d}w$ is constant, one has $\nabla E(x(w_k))$

$= 0$, such that the $x(w_k)$ are critical points of the energy. It is now easy to test if a path x is a least-action path by calculating the action (eq. 1) along the path and comparing it to the right-hand side of eq. (12). Interestingly, by standard methods in differential geometry (Do Carmo 2016), condition (10) can be shown to imply that x is a geodesic on the energy manifold. Thus, a geodesic connecting two local energy minima achieves equality in eq. (12).

2.6 Morse theory

Topologically different critical points in multidimensions are distinguished by their *Morse index*, which is defined as the dimension n_- of the submanifold on which the Hessian is negative definite, such that on this submanifold the critical point is a maximum. Intuitively, the Morse index of the highest saddle point along the optimal transition path should not be too large, because, apart from singular cases, the action is minimized along only 1-D manifold, that is, an isolated path parallel to the gradient which connects initial and final minima. Therefore, if at the highest saddle point the Morse index is $n_- > 1$, the other $n_- - 1$ descending directions should lead into different LEM states. The choice for these LEM states should not be too large whenever the initial and final minima are close to the global energy minimum.

On the other hand, the micromagnetic energy landscape for models involving a large number of magnetization variables will inevitably have a huge number of saddle points. This can be shown by a general result of Morse theory (Milnor 1963) which implies that for a 2-D energy surface with Euler characteristic χ_{Euler}, the numbers N_{min} of minima, N_{max} of maxima and N_{saddle} of saddle points are connected by the relation:

$$N_{\text{min}} + N_{\text{max}} - N_{\text{saddle}} = \chi_{\text{Euler}}. \tag{13}$$

For a sphere, representing all possible magnetization directions of a single spin, the Euler characteristic is $\chi_{\text{Euler}} = 2$.

The generalization of eq. (13) to any finite-dimensional compact manifold is the *Morse relation* (Milnor 1963):

$$\sum_{k=0}^{N} (-1)^k N_k = \chi_{\text{Euler}}. \tag{14}$$

Here N_k is the number of critical points with Morse index k, which means that the negative definite submanifold has dimension $n_- = k$. For a micromagnetic energy that depends on N magnetization directions, the manifold of all possible magnetization states is a direct product of N 2-D spheres, therefore $\chi_{\text{Euler}} = 2^N$. On this $2N$-dimensional manifold we get from eq. (14):

$$N_{\text{min}} + N_{\text{max}} + N_{\text{even}} - N_{\text{odd}} = 2^N, \tag{15}$$

where N_{even} and N_{odd} are the number of true saddle points with even or odd Morse index, respectively.

If this manifold describes an ensemble of interacting SD grains, each grain has at least two critical points, minima or maxima, in zero external field. If interaction is weak, the total energy of the system inherits almost all these minima and maxima as saddle points. Thus, it is understandable that the total number of critical points exceeds even a huge figure like 2^N.

The situation is different if the $2N$-dimensional manifold describes an exchange coupled grain with inhomogeneous magnetization structure, like in most micromagnetic applications. In this case, it turns out that only a limited number of minima and maxima, like flower or vortex states, exist. According to eq. (15), there must appear an enormous number of true saddle points with even Morse index, that is, not 1-D lines.

Thus, inevitably there exist a large number of paths, with different action S, which connect the local minima and complicate the search of the lowest action path. Another circumstance causing difficulties to find path lines by numerical means is that the field lines passing through the saddle points form submanifolds of zero measure. In other words, the saddle points are unstable in the sense that almost all field lines in their vicinity are deflected aside (except for those which go directly through the saddle point).

2.7 Euler–Lagrange path relaxation

To numerically calculate the optimal geometric transition path, one would like to start from an arbitrarily chosen initial path p_0 which then is iteratively improved by some updating scheme. A heuristic procedure is known as NEB technique. Here we derive an optimal updating scheme which corresponds to a gradient minimization of minimal path action. To this end, we follow the standard derivation of the Euler–Lagrange equation to prove that the change δS_{min} in action due to a variation δx in the path is given by

$$\delta S_{\text{min}} = 2 \int_0^L \left(\nabla \|\nabla E\| - \|\nabla E\| \frac{\mathrm{d}^2 x}{\mathrm{d}s^2} \right) \delta x \, \mathrm{d}s. \tag{16}$$

The direction of maximal increase in S_{min} now is a function $\delta * x \in L_2([0, L])$ with $\|\delta * x\|_2 = 1$ which maximizes eq. (16). By Cauchy's inequality

$$\delta^* x = \frac{\nabla \|\nabla E\| - \|\nabla E\| \frac{\mathrm{d}^2 x}{\mathrm{d}s^2}}{\left\| \nabla \|\nabla E\| - \|\nabla E\| \frac{\mathrm{d}^2 x}{\mathrm{d}s^2} \right\|_2}. \tag{17}$$

The optimal Euler–Lagrange relaxation towards a minimal action path accordingly is given by

$$x_n := x_{n-1} - \alpha \, \delta^* x_{n-1}, \tag{18}$$

for a sufficiently small positive step size α. For a numerical evaluation eq. (17) is disappointing, because it requires calculation of second derivatives of E, which is very time consuming for large numbers of variables. Interestingly, the updating depends only on the norm $\|\nabla E\|$ and not explicitly on E or the vector ∇E. And second, the term involving $\mathrm{d}^2 x/\mathrm{d}s^2$ enforces a reduction of local curvature in regions where $\|\nabla E\| > 0$. This straightens out the path in proportion to the energy-gradient norm during the update and thus avoids the formation of kinks which are a common problem in NEB algorithms (Henkelman *et al.* 2000b). Only at critical points, where $\|\nabla E\| = 0$ the final least-action path is not iteratively smoothed out and corners could form, whereby the final path may not be differentiable only at critical points.

2.8 Relation between action and path relaxation

The heuristic scheme of NEB optimization finds a path between two minima across a saddle point in multidimensional energy landscapes, by exploiting the fact that there is such a path which everywhere runs along the energy gradient. Starting from an arbitrary initial path $x_0(s)$ it is thus attempted to adjust the path towards the direction along the negative energy gradient, but perpendicular to the local tangent. This relaxation scheme can be analytically described as the solution of a boundary value problem for a system of

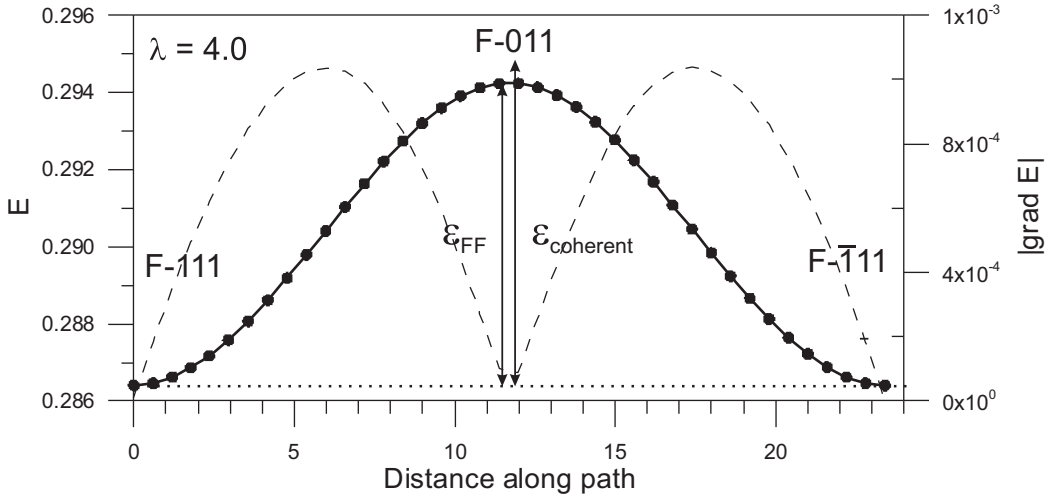

Figure 1. Energy variation across the optimal transition from an F-111 flower state to an F-$\bar{1}$1 vortex state at $\lambda = 4.0$. Each circle represents an intermediate magnetization state used for the calculation. The dashed line corresponds to the absolute value of the energy gradient along the transition path. The maximum energy state along the path is the F-011 flower state. The 3-D micromagnetic calculation ($\epsilon_{\rm FF}$) leads only to a minor decrease of the energy barrier with respect to coherent rotation ($\epsilon_{\rm coherent}$). This improvement results from the small spin deflections close to the particle surface.

Table 1. Normalized initial energies E and energy barriers ϵ for numerically calculated optimal transitions between listed initial and final states for $Q = -0.1$ and different values of λ.

λ	Initial state	Initial energy E	Intermediate state	Barrier ϵ
4.0	F-111	0.286404	F-110	0.007825
4.5	F-111	0.28308	V-011	0.005417
4.5	F-111	0.28308	F-011	0.008172
4.5	F-111	0.28308	V-001	0.011041

Table 2. Normalized energy barriers for optimal transitions between a reduced set of initial and final states for $Q = -0.1$ and $\lambda = 5.0$. Transitions with the same initial state are listed in the same column. Transitions with the same final state are listed in the same line. The corresponding complete set of 60 LEM states is obtained by taking into account cubic symmetry leading to 8 states of class F-111 or V-111, 6 states of class V-001 and 12 states of class V-110. In addition, all vortex states exist in two varieties of different helicities.

	V-001	V-110	V-111	F-111
V-001	0	0.000123	0.001389	0.00349
V-110	0.006263	0	0.000598	0.002925
V-111	0.008297	0.001368	0	0.003836
F-111	0.012117	0.005521	0.005665	0

nonlinear partial differential equations

$$\frac{\partial x}{\partial u}(u,s) = -\nabla E + \frac{\langle \frac{\partial x}{\partial s}, \nabla E\rangle}{\|\frac{\partial x}{\partial s}\|^2}\,\frac{\partial x}{\partial s}, \tag{19}$$

with the boundary conditions

$$x(0,s) = x_0(s), x(u,0) = x_0(0), x(u,L) = x_0(L). \tag{20}$$

There are two main differences between the NEB relaxation (eq. 19) and the correct action relaxation (eq. 9). While the correct equation only depends on $\|\nabla E\|$, the NEB relaxation explicitly depends on the vector ∇E, and the NEB equation does not use the second derivative of x to avoid the formation of kinks. Any unnecessary curvature in $x_0(s)$ therefore tends to become folded up by the evolution according to eq. (19) into back-and-forth movements along the final path. NEB algorithms apply different heuristic schemes to avoid this behaviour, but it is unclear to which extent these empirical corrections can deteriorate the path optimization. In the here described numerical scheme, this is tested by checking whether the iteratively improved paths decrease the action (eq. 1). Equality in eq. (12) then even provides an absolute stopping criterion for the path minimization.

3 A MODIFIED RELAXATION METHOD TO DETERMINE TRANSITION PATHS FROM MICROMAGNETIC MODELS

3.1 Definitions

A micromagnetic structure m is determined by K magnetization vectors on a special grid over the particle. Each magnetization vector is a unit vector determined by two polar angles θ, ϕ. The distance $d(m_1, m_2)$ between two magnetization structures is defined by

$$d(m_1,m_2) := \left[\frac{1}{V}\int_V \arccos^2(m_1(r)\cdot m_2(r))\,{\rm d}V\right]^{1/2}. \tag{21}$$

The local direction vector from m_1 to m_2 is the gradient

$$v(m_1,m_2) := -\nabla d(\,.\,,m_2)(m_1). \tag{22}$$

If two magnetization structures m_0 and m_1 contain no opposite directions, that is, for all $r \in V$ we have $m_0(r) \neq -m_1(r)$, then it is possible to linearly interpolate between m_0 and m_1 by defining $m_t(m_0, m_1), (r)$ as the intermediate vector on the smaller great circle segment connecting $m_0(r)$ and $m_1(r)$ which has angular distance $t\arccos(m_0(r)\cdot m_1(r))$ from $m_0(r)$.

By minimization of $E(m)$ using gradient information $\nabla E(m)$ an initial minimum m_A and a final minimum m_B are found.

3.2 Outline of the relaxation procedure

In summary, the results of the previous section show that the transition probability between m_A and m_B is in very good approximation determined by the minimal energy barrier between them. This barrier is achieved along some optimal geometrical least-action path

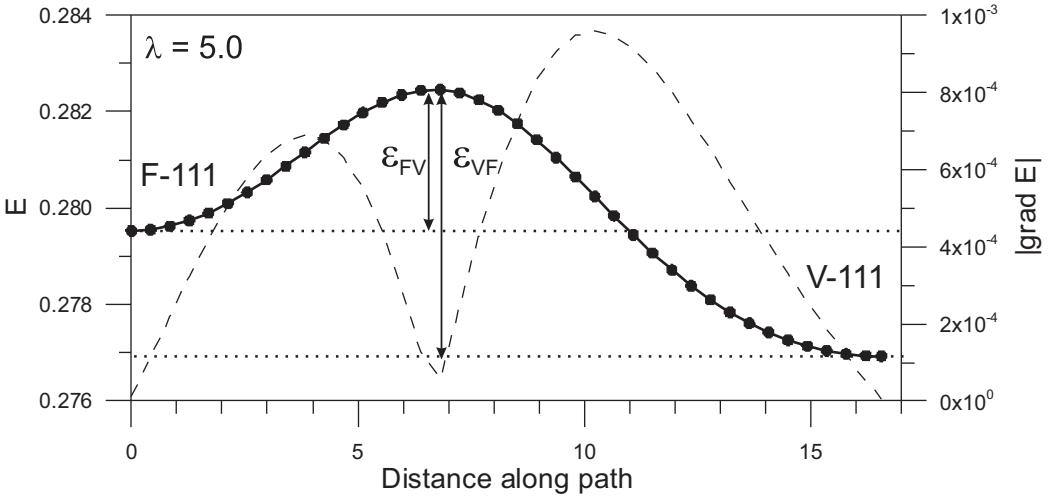

Figure 2. Energy variation across the optimal transition from an F-111 flower state to a V-111 vortex state at $\lambda = 5.0$. Each circle represents an intermediate magnetization state used for the calculation. The dashed line corresponds to the absolute value of the energy gradient along the transition path. Because the energies of F-111 and V-111 are different, also the energy barriers for a transition from F-111 to V-111 (ϵ_{FV}) and from V-111 to F-111 (ϵ_{VF}) differ.

Table 3. Normalized energy barriers for optimal transitions between vortex states for $Q = -0.1$ and $\lambda = 6.0$–8.0. While V-111 is a marginally stable LEM at $\lambda = 6.0$, it is unstable for $\lambda = 7.0, 8.0$. Types of V-100 vortex states are the global energy minima at these grain sizes and the energy barrier refers to a symmetric transition between two adjacent states of this type, for example, V-100–V-010.

λ	Initial state	Intermediate state	Barrier ϵ
6.0	V-100	V-111	0.009486
7.0	V-100	V-111	0.006372
8.0	V-100	V-111	0.005876

$m(s)$ with $m(0) = m_A$ and $m(1) = m_B$ which also represents the most likely transition path. The state of maximal energy along this path is a saddle point of the total energy function $E(m)$ and the least action path is everywhere parallel to $\nabla E(m)$. To find this optimal transition path, we propose a relaxation method which combines the advantages of the NEB technique of Dittrich *et al.* (2002) with the additional action minimization of Berkov (1998b). Two techniques are required for finding the optimal path by means of iterative relaxation:

(1) An updating scheme which determines an improved transition path $m^{k+1}(s)$ from a previous path $m^k(s)$.
(2) A method of finding an initial transition path $m^0(s)$ within the basin of attraction of the optimal path.

The here proposed updating scheme starts from an initial path $m^0(s)$ which is determined by interpolating N intermediate states $m^0(s_j)$ which correspond to the magnetization structures at the s-coordinates $0 = s_1 < s_2 < \ldots < s_N = 1$ for $j = 1, \ldots, N$. For the interpolation to be well defined, N is required to be large enough to ensure that neighbouring structures $m^k(s_j)$ and $m^k(s_{j+1})$ never contain opposite magnetization vectors. Similar to the NEB method, in step k the path $m^k(s)$ is changed according to

$$m^{k+1}(s) := m^k(s) - \alpha_k \left[\nabla E(m^k(s)) - \left(\nabla E(m^k(s)) \cdot t^k(s)\right) t^k(s)\right], \quad (23)$$

where $t^k(s)$ is the tangent vector to the path $m^k(s)$ at s and $\alpha_k > 0$ is a real number. This updating scheme moves the path downwards along the part of the energy gradient which is perpendicular to path itself. This algorithm converges to a path which is almost everywhere parallel to ∇E. However, eq. (23) describes not a true gradient descent for the action, and the final path may not achieve minimal action due to the formation of kinks during the minimization (Henkelman & Jónsson 2000a; Henkelman *et al.* 2000b; Dittrich *et al.* 2002).

The here proposed method differs from previous NEB techniques in two details: first, α_k is chosen such that $S(m^{k+1}) < S(m^k)$. This ensures that the action decreases in each step. Second, α_k is dynamically adapted to achieve rapid convergence. The following procedure to choose α_k fulfils both aims.

3.2.1 *Adaption of* α_k

Starting with the initial value $\alpha_0 = 1$, it is evaluated after each step whether the action of the updated path is decreased, that is, $S(m^{k+1}(s)) < S(m^k(s))$. While this is true, the new value $\alpha_{k+1} = \alpha_k$ is kept constant, but only for at most five steps. In this phase, eq. (23) performs a quasi-gradient descent 'creeping' towards the optimal path. Afterwards, if S still decreases, we set $\alpha_{k+1} = 2\,\alpha_k$ in each following step until some $S(m^{k+1}(s)) > S(m^k(s))$. This phase can be interpreted as an 'accelerated steepest descent'.

If at any time $S(m^{k+1}(s)) > S(m^k(s))$, the path $m^{k+1}(s)$ is rejected and eq. (23) is evaluated for a new α_{k+1} value of $\alpha_{k+1} = 1/4\,\alpha_k$. This behaviour avoids 'overshooting' of the gradient descent and all our tests show that this iterative adaption of α_k leads to a much faster convergence than choosing any fix value $\alpha_k = \alpha$.

By comparing the achieved action $S(m^k(s))$ to $S_{\min}$ from eq. (12) during the relaxation, it is possible to detect the formation of kinks and to decide when the minimization succeeds. This action criterion is better than testing whether the final path is parallel to ∇E, since the latter is also true for paths with kinks.

3.3 Determination of the initial path

Since the relaxation scheme works similar to a gradient minimization algorithm, it adjusts to the next local optimum of the action function. Therefore, the choice of the initial path is crucial for obtaining the globally optimal path. Here, we propose a method to

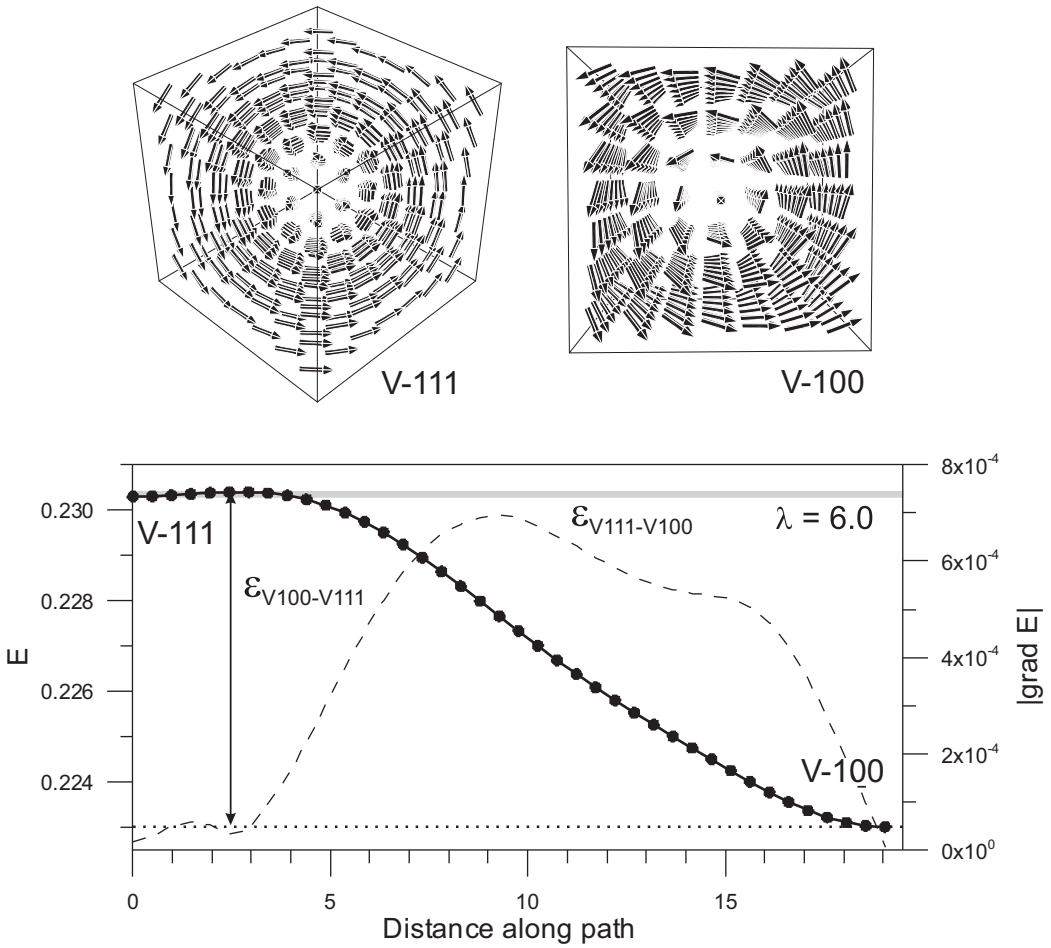

Figure 3. Energy variation across the transition from a V-111 flower state to a V-100 vortex state at $\lambda = 6.0$. The top figures show the magnetization structure of the V-111 state as seen along the ⟨111⟩-direction and the V-100 vortex as seen along the ⟨100⟩-direction. In the bottom diagram again each circle represents an intermediate magnetization state used for the calculation. The dashed line corresponds to the absolute value of the energy gradient along the transition path. The tiny energy barrier $\epsilon_{\mathrm{V111–V100}}$ in relation to $\epsilon_{\mathrm{V100–V111}}$ indicates that the V-111 state is a very unstable LEM as compared to V-100. However, it is important for the transition between the more stable vortex states. For example, the optimal transition from V-001 to V-100 is a combination of the symmetric vortex rotations V-001–V-111 and the shown transition V111–V100.

Table 4. Minimal energy density ϵ or absolute energy E_{b} necessary to leave the global energy minima for different values of λ. m is the reduced magnetization at the global minimum.

λ	ϵ	E_{b}	m
4.0	0.007825	0.5008	0.991297
4.5	0.005417	0.49362	0.986527
5.0	0.006263	0.782875	0.705928
6.0	0.009486	2.048976	0.509672
7.0	0.006372	2.185596	0.310451
8.0	0.005876	3.008517	

find a good initial path $m^0(s)$ by a sequence of minimizations of modified energy functions.

For parameters μ, β, ϵ and Δ we consider the modified energy function

$$E^*_\Delta(m) = E(m) + \mu\,[d(m, m_A) - \Delta]^2 + \frac{\beta}{d(m, m_B) + \varepsilon}. \qquad (24)$$

The parameters μ, β and ϵ are chosen such that for $\Delta = d(m_B, m_A)$, the final state m_B is a unique optimum of $E^*_\Delta(m)$, while for m with $d(m, m_A) \ll d(m_B, m_A)$ the last term of $E^*_\Delta(m)$ is small in comparison to $E(m)$. The value of μ should be large enough to ensure that the distance between m_A and the minimum of E^*_Δ is indeed close to Δ.

Now a sequence m^0_j, $j = 1, \ldots, J$ of magnetization structures is iteratively obtained by setting $m^0_0 = m_A$ and m^0_j to the result of minimizing $E^*_{\Delta_j}(m)$, where $\Delta_j = j/J\, d(m_B, m_A)$.

Interpolating between the structures m^0_j determines an initial path which (1) starts in m_A and ends in m_B, (2) has relatively equally spaced intermediate states m^0_j and (3) prefers intermediate states m^0_j at distance Δ_j with low energy $E(m)$.

4 ENERGY BARRIERS IN A CUBIC PSEUDO-SINGLE DOMAIN PARTICLE

4.1 Numerical calculations, material constants and normalization

All numerical calculations reported here, are based on a Fast-Fourier transform (FFT) accelerated 3-D micromagnetic algorithm as described in Fabian *et al.* (1996). This algorithm and the subsequent path optimization are implemented in Mathematica. They are performed in terms of normalized material parameters as defined in

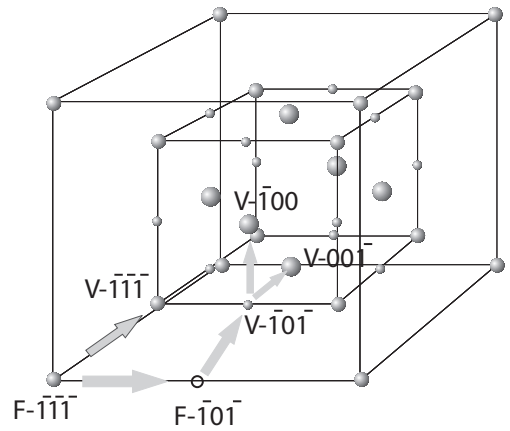

Figure 4. Schematic representation of transition paths in magnetization space for a cubic particle with $\lambda = 5.0$. Each sphere corresponds to the magnetization of an LEM state, whereby larger spheres represent lower minima, the open circle represents a transition state that is no minimum. The cubic structure reflects the cubic symmetry of the particle. Grey arrows indicate two of the many possible transition paths (or decay modes): (1) a direct decay form F-$\bar{1}\bar{1}\bar{1}$ to V-$\bar{1}\bar{1}\bar{1}$; (2) indirect decay from F-$\bar{1}\bar{1}\bar{1}$ over an unstable intermediate F-$\bar{1}$0$\bar{1}$ state into V-$\bar{1}$0$\bar{1}$ and further to either V-$\bar{1}$00 or V-00$\bar{1}$. Note that each sphere in principle represents two vortex states of inverse helicity (R and L). However, transitions between vortex states of different helicities have large energy barriers and can be neglected.

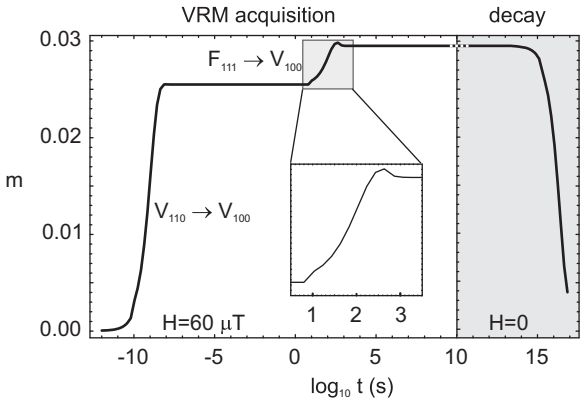

Figure 5. Modelled acquisition of viscous magnetization in the cubic particle with $\lambda = 5.0$. The initial state is an equidistribution over all possible LEM states with zero net magnetization. In a small external field, the first acquisition process is the immediate decay from V-110 type states into V-100 type states, which occurs within about 10^{-9} s. Due to the field induced asymmetry of the energy barriers, a remanence is acquired during this process. The second process is a decay of F-111 type states into V-100 type states. This occurs between about 10^2 and 10^3 s and shows an intermediate overshooting of remanence.

Hubert & Schäfer (1998). Magnetic hardness Q, in case of cubic magnetocrystalline anisotropy, is the numerical ratio $Q = K_1/K_d$, where

$$K_d = \frac{1}{2}\mu_0 M_s^2$$

is the characteristic magnetostatic self-energy in terms of saturation magnetization M_s and K_1 is the first cubic anisotropy constant. The exchange length $\lambda = \sqrt{A/K_d}$ determines the characteristic length scale above which magnetostatic self-energy is able to overcome the quantum mechanical exchange coupling between neighbouring spins, represented by the exchange constant A. For magnetite these material constants are $M_s = 480$ kA m^{-1}, $A = 1.32 \times 10^{-11}$ J m^{-1} and $K_1 = -1.25 \times 10^4$ J m^{-3}. Accordingly, $K_d = 145$ kJ m^{-3}, $\lambda_{ex} = 9.55$ nm and magnetic hardness is $Q = -0.0863$. Unless otherwise stated, all results in the following subsections are obtained for the magnetite-like value $Q = -0.1$. Lengths λ are given in units of λ_{ex}, and energy densities are normalized to K_d.

4.2 Potential barriers in cubic particles

Numerically calculated energy barriers ϵ in Table 1 report switching processes between SD-like flower states. A typical result is displayed in Fig. 1. Compared to the case of coherently rotating SD magnetization, where $\epsilon_{SD} = 1/120 = 0.008333$, all numerically optimized barriers are clearly lower, especially for $\lambda = 4.5$. For $\lambda = 4.0$ the optimal transition is still close to coherent rotation of all spins, because the magnetization structure at the optimal saddle point is F-110 (flower state with magnetization in [110] direction) and almost homogeneous. For $\lambda = 4.5$, the magnetization structure at the optimal saddle point is V-011 (vortex with vortex core in [011] direction), and this intermediate vortex state substantially reduces the energy barrier in comparison to other locally optimal transition paths with intermediate states F-011 or V-001 (Table 1).

For $\lambda = 5.0$ in Table 2, the situation is most complex, because there are a number of competitive LEM-states with similar energy: V001 with $E = 0.27079$, V110 with $E = 0.\ 276931$, V111 with $E = 0.277701$ and F111 with $E = 0.279527$. Consequently, there are no direct transitions between topologically identical states like V-001 and V-010. Such transitions were the only ones observed for $\lambda = 4.0$ and $\lambda = 4.5$. For $\lambda = 5.0$ the state V-001 can change to V-010 only indirectly, either through V-111 or V-011 or F-111. A transition between F-111 and V-111 is displayed in Fig. 2.

For $\lambda \geq 6.0$ in Table 3, the situation becomes simple again, because now the only stable states are vortices, like the face-centred V-001. A transition between a nearly unstable diagonal vortex V-111 and the absolute energy minimum V-100 for $\lambda = 6.0$ is shown in Fig. 3. The absolute thermoactivation barriers $E_b = \varepsilon \lambda^3$ for the most stable LEM states are listed in Table 4. These are F-111 states for $\lambda \leq 4.5$ and V-001 states for $\lambda \geq 5.0$. These absolute energy barriers have a minimum at $\lambda = 4.5$ near the flower–vortex boundary, corresponding to previous findings that the thermal stability of large SD particles can deteriorate (Winklhofer *et al.* 1997; Shah *et al.* 2018).

4.3 Statistical theory of multidomain viscous remanent magnetization

The first application of the above presented calculation of energy barriers is a complete description of low-field viscous magnetization processes in a micromagnetically modelled cubic particle. Knowing the optimal transition paths between all LEM structures S_i of the investigated particle allows for calculating the zero field temporal isothermal transition matrix $M(\Delta t)$, which describes the continuous homogeneous Markov process of random thermally activated transitions between all possible states:

$$M(\Delta t) \equiv \mathbb{P}\left[S(t) = S_j \wedge S(t + \Delta t) = S_i\right] = \exp\left[\mu\, \Delta t\right]. \qquad (25)$$

Here, the matrix elements μ_{ij} of the infinitesimal generator of the semi-group $M(t)$ are given by the relative outflow from S_j to S_i for $i \neq j$. The relative inflow from all other states determines the diagonal

element μ_{ii}.

$$\mu_{ij} = -\frac{\Delta E_{ij}}{k_B T\, \tau_0} \text{for } i \neq j \tag{26}$$

$$\mu_{ii} = -\sum_{i \neq j} \mu_{ji}. \tag{27}$$

Once, the μ_{ij} have been calculated, it is easily possible to determine the viscous decay of any initial probability distribution $\rho_i^0 \equiv \mathbb{P}[S_0 = S_i]$ by multiplication with the time evolution matrix exponential

$$\rho(t) = \exp[\mu\, t]\ \rho_i^0. \tag{28}$$

Multiplication by the corresponding magnetizations m_i of states S_i yields the viscous evolution of remanence

$$m(t) = \sum_i m_i\, \rho_i(t). \tag{29}$$

When a small field H is applied, the energy barrier E_b^{ij} in first order changes according to

$$E_b^{ij}(H) = E_b^{ij} + (m_j - m_{ij}^{\max})\, H, \tag{30}$$

where $m_{ij}^{\max}$ denotes the magnetization at the maximum energy state along the optimal transition path from S_i to S_j. The approximation used to obtain eq. (30) assumes that H is so small that it does not change the magnetization structures of the LEM and saddle-point states notably. Only the field induced energy is taken into account. It is easily seen that all other energy changes are of second order in H.

Using the in-field energy barriers it is straightforward to determine the matrix exponential which governs viscous remanent magnetization (VRM) acquisition. By defining

$$\mu_{ij}(H) = -\frac{E_b^{ij}(H)}{k_B T\, \tau_0} \text{for } i \neq j \tag{31}$$

$$\mu_{ii}(H) = -\sum_{i \neq j} \mu_{ji}(H), \tag{32}$$

the above zero field theory directly extends to sufficiently weak fields. For the above cubic PSD particle, all matrices are of size 60 $\times$ 60 and the calculations have been performed by a Mathematica program.

5 VISCOUS MAGNETIZATION

5.1 Viscous remanence acquisition and decay in an ensemble of cubic PSD magnetite

Using the above mathematical methods it is possible to calculate the statistics of viscous remanence acquisition and decay for our single PSD particle with respect to any field vector of sufficiently small length H. In order to model an isotropic ensemble, it is necessary to average the VRM properties over all possible field directions. This has been approximated by drawing 20 random directions from an equidistribution over the unit sphere and averaging the modelled VRM acquisition and decay curves. For room temperature this yielded the ensemble curve as shown in Fig. 5.

The left-hand side of Fig. 5 shows the remanence acquisition in a modelled field of $H = 60\ \mu$T when starting from an initial state ρ_0 at $t = 0$ which assigns equal probability to all existing LEM states. Already within 10^{-9} s the remanence increases rapidly due to the immediate depletion of the nearly unstable V-110 vortex states which decay into the stable V-100 states (see Table 2). The remanence forms because in zero field there are two equally probable transitions, for example, V-110 $\rightarrow$ V-100 and V-110 $\rightarrow$ V-010. Within the external field one of these decay paths becomes more probable which leads to a relative overpopulation of the field aligned V-100 type states. Nearly synchronously there occurs a two-step process V-111 $\rightarrow$ V-110 $\rightarrow$ V-100. It is controlled by the somewhat slower transition V-111 $\rightarrow$ V-110, but still both take place within the first few 10^{-9} s. The last VRM acquisition processes occurs only after a much longer waiting time of 10–10^3 s. First the initial F-111 type states transform via F-110 type states into V-110 type states which then immediately decay into V-100 (Fig. 4). This last process produces an astonishing remanence overshooting as displayed in Fig. 5: the remanence during the VRM acquisition process is for a certain time higher than the finally obtained equilibrium VRM. This is not an artefact of the modelling, but can be explained by a real physical process. The reason is that during VRM acquisition the metastable flower states are decaying into V-100 states at different rates, depending on whether they are aligned or misaligned to the external field. Because the field-aligned states are decaying slower than the misaligned states, there is a short time window during which the field-aligned flower states outweigh the misaligned states and generate a visibly higher magnetization than the later vortex states into which they decay.

The right-hand side of Fig. 5 shows that when the field is switched off after VRM acquisition, the obtained remanence is carried only by extremely stable V-100 type states which require a theoretical waiting time of 10^{15} s to equilibrate into a zero remanence state.

5.2 High stability of PSD VRM

Extremely stable VRM has been observed in palaeomagnetic studies and domain observations (De Groot *et al.* 2014). The above mechanisms give a theoretical explanation how high stability of VRM intrinsically occurs in PSD particle ensembles. The basic process is the relaxation of naturally produced metastable states into stable ones. Additional mechanisms in multidomain VRM acquisition, like stress relaxation by dislocation creep (Williams & Muxworthy 2006), are certainly of importance, but have to be considered on the background of the here described intrinsic mechanisms.

Metastable states occur by TRM acquisition in PSD ensembles where the cooling rate is fast enough to stabilize metastable flower states. A long-term VRM, acquired in the field after cooling and carried by newly formed vortex states, then is extremely stable and can significantly bias palaeomagnetic measurements, especially palaeointensity determinations.

Laboratory alternating field (AF) demagnetization rather leads to a more stable LEM state (perhaps even the GEM) because the magnetization structure is provided with a lot of energy which is stepwise reduced. Thus AF-demagnetization would rather end up in a vortex state for a PSD particle (Dunlop & Argyle 1997; Witt *et al.* 2005).

During natural chemo-viscous magnetization by crystal growth, a grain changes sequential from the SP state into a stable SD and later a PSD state. The first stable SD state is almost homogeneously magnetized along a ⟨111⟩-axis. It then transforms in a more developed flower state which then becomes metastable as soon as the vortex has lower energy. At this point, the process of VRM acquisition will start to produce extremely stable remanences.

6 CONCLUSIONS

An efficient and fast combination of an NEB and an action-minimization technique has been designed and tested to calculate optimal transition paths in complex micromagnetic models. The corresponding algorithm is now implemented within the MERRILL micromagnetic code (Ó Conbhuí *et al.* 2018), and can be used to evaluate arbitrary transitions between local energy minima in PSD particles. Based on methods developed in Fabian (2003) and Newell (2006), VRM acquisition in an isotropic PSD ensemble was calculated as a spherical average over the related homogeneous continuous Markov processes. In the modelled particle ensemble, a physically meaningful overshooting of magnetization during VRM acquisition has been found. The result that VRM acquisition in PSD particles can be much faster than VRM decay explains for findings of extremely stable VRM in palaeomagnetic studies.

ACKNOWLEDGEMENTS

KF received funding through NGU and the Centre of Excellence: Arctic Gas hydrate, Environment and Climate (CAGE) funded by the Norwegian Research Council (Grant No. 223259). VS received financial support from state assignment of IPE RAS. We gratefully acknowledge thoughtful reviews by A. Muxworthy and an anonymous referee.

REFERENCES

Berkov, D., 1998a. Evaluation of the energy barrier distribution in many-particle systems using the path integral approach, *J. Phys.: Condens. Matter,* **10,** L89–L95.

Berkov, D., 1998b. Numerical calculation of the energy barrier distribution in disordered many-particle systems: the path integral method, *J. Magn. Magn. Mater.,* **186,** 199–213.

Berkov, D., 1998c. Calculation of the energy barriers in strongly interacting many-particle systems, *J. Appl. Phys.,* **83,** 7390–7392.

De Groot, L.V., Fabian, K., Bakelaar, I.A. & Dekkers, M.J., 2014. Magnetic force microscopy reveals meta-stable magnetic domain states that prevent reliable absolute palaeointensity experiments, *Nat. Commun.,* **5,** doi:10.1038/ncomms5548.

Dittrich, R., Schrefl, T., Suess, D., Scholz, W., Forster, H. & Fidler, J., 2002. A path method for finding energy barriers and minimum energy paths in complex micromagnetic systems, *J. Magn. Magn. Mater.,* **250,** L12–L19.

Do Carmo, M.P., 2016. *Differential Geometry of Curves and Surfaces,* 2nd edn, Dover.

Dunlop, D.J. & Argyle, K.S., 1997. Thermoremanence, anhysteretic remanence and susceptibility of submicron magnetites: nonlinear field dependence and variation with grain size, *J. geophys. Res.,* **102**(B9), 20 199–20 210.

Einsle, J.F. *et al.*, 2016. Multi-scale three-dimensional characterization of iron particles in dusty olivine: implications for paleomagnetism of chondritic meteorites, *Am. Mineral.,* **101** (9-10), 2070–2084.

Enkin, R.J. & Dunlop, D.J., 1988. The demagnetization temperature necessary to remove viscous remanent magnetization, *Geophys. Res. Lett.,* **15,** 514–517.

Enkin, R.J. & Williams, W., 1994. Three-dimensional micromagnetic analysis of stability in fine magnetic grains, *J. geophys. Res.,* **99,** 611–618.

Fabian, K., 2003. Statistical theory of weak field thermoremanent magnetization in multidomain particle ensembles, *Geophys. J. Int.,* **155,** 479–488.

Fabian, K., Kirchner, A., Williams, W., Heider, F., Leibl, T. & Hubert, A., 1996. Three-dimensional micromagnetic calculations for magnetite using FFT, *Geophys. J. Int.,* **124,** 89–104.

Graham, R., 1975. Macroscopic theory of fluctuations and instabilities in optics and hydrodynamics, in *Fluctuations, Instabilities and Phase Transitions,* pp. 215–279, ed. Riste, T., Plenum.

Henkelman, G. & Jónsson, H., 2000a. Improved tangent estimate in the nudged elastic band method for finding minimum energy paths and saddle points, *J. Chem. Phys.,* **113,** 9978–9985.

Henkelman, G., Uberuaga, B.P. & Jónsson, H., 2000b. A climbing image nudged elastic band method for finding saddle points and minimum energy paths, *J. Chem. Phys.,* **113,** 9901–9904.

Hubert, A. & Schäfer, R., 1998. *Magnetic Domains,* 1st edn, Springer-Verlag.

Milnor, J., 1963. *Morse Theory,* Princeton University Press.

Muxworthy, A.R., Dunlop, D.J. & Williams, W., 2003. High-temperature magnetic stability of small magnetite particles, *J. geophys. Res.,* **108,** 2281, doi:10.1029/2002JB002195.

Nagy, L., Williams, W., Muxworthy, A.R., Fabian, K., Almeida, T.P., ÓConbhui, P. & Shcherbakov, V.P., 2017. Stability of equidimensional pseudo-single-domain magnetite over billion-year timescales, *Proc. Natl. Acad. Sci. USA,* **114**(39), 10 356–10 360.

Newell, A.J., 2006. Superparamagnetic relaxation times for mixed anisotropy and high energy barriers with intermediate to high damping: 1. Uniaxial axis in a <001 > direction, *Geochem. Geophys. Geosyst.,* **7**(3), doi:10.1029/2005GC001146.

Ó Conbhuí, P., Williams, W., Fabian, K., Ridley, P., Nagy, L. & Muxworthy, A.R., 2018. MERRILL: micromagnetic Earth related robust interpreted language laboratory, *Geochem. Geophys. Geosyst.,* **19**(4), 1080–1106.

Olsen, R.A., Kroes, G.J., Henkelman, G., Arnaldsson, A. & Jónsson, H., 2004. Comparison of methods for finding saddle points without knowledge of the final states, *J. Chem. Phys.,* **121,** 9776–9792.

Onsager, L. & Machlup, S., 1953. Fluctuations and irreversible processes, *Phys. Rev.,* **91,** 1505–1515.

Rave, W., Fabian, K. & Hubert, A., 1998. Magnetic states of small cubic particles with uniaxial anisotropy, *J. Magn. Magn. Mater.,* **190,** 332–348.

Shah, J. *et al.*, 2018. The oldest magnetic record in our solar system identified using nanometric imaging and numerical modeling, *Nat. Commun.,* **9,** doi:10.1038/s41467-018-03613-1.

Thomson, L.C., Enkin, R.J. & Williams, W., 1994. Simulated annealing of three-dimensional micomagnetic structures and simulated thermoremanent magnetization, *J. geophys. Res.,* **99,** 603–609.

Valdez-Grijalva, M.A., Nagy, L., Muxworthy, A.R., Williams, W. & Fabian, K., 2018. The magnetic structure and palaeomagnetic recording fidelity of sub-micron greigite (Fe_3S_4), *Earth planet. Sci. Lett.,* **483,** 76–89.

Williams, W. & Dunlop, D.J., 1989. Three-dimensional micromagnetic modelling of ferromagnetic domain structure, *Nature,* **337,** 634–637.

Williams, W. & Muxworthy, A.R., 2006. Understanding viscous magnetization of multidomain magnetite, *J. geophys. Res.,* **111**(B2), doi:10.1029/2005JB003695.

Winklhofer, M., Fabian, K. & Heider, F., 1997. Magnetic blocking temperature of magnetite calculated with a three-dimensional micromagnetic model, *J. geophys. Res.,* **102,** 22 695–22 709.

Witt, A., Fabian, K. & Bleil, U., 2005. Three-dimensional micromagnetic calculations for naturally shaped magnetite: octahedra and magnetosomes, *Earth planet. Sci. Lett.,* **233**(3–4), 311–324.

APPENDIX: EULER-–LAGRANGE EQUATION FOR GEOMETRIC ACTION MINIMIZATION

To efficiently derive the Euler–Lagrange equation for geometric action minimization it is convenient to use tensor calculus including Einstein's sum convention. For comparison with classical physics, the variable w is interpreted as a time t and the path x as a generalized variable q.

We then have to apply the Euler–Lagrange operator $\frac{\partial}{\partial q} - \frac{\mathrm{d}}{\mathrm{d}t}\frac{\partial}{\partial \dot{q}}$ to the Lagrange function $L(q, \dot{q}) = \sqrt{g_i\, g_i}\,\sqrt{\dot{q}_i \dot{q}_i}$, where $g_i = \partial_i E(q)$. This needs the following expressions:

$$\dot{\partial}_k \|\dot{q}\| := \frac{\partial}{\partial \dot{q}_k}\sqrt{\dot{q}_i \dot{q}_i} = \frac{\dot{q}_k}{\|\dot{q}\|} \tag{A1}$$

$$\frac{d}{dt}\,\dot{\partial}_k \|\dot{q}\| = \frac{\mathrm{d}}{\mathrm{d}t}\,\frac{\dot{q}_k}{\|\dot{q}\|} = \frac{\ddot{q}_k}{\|\dot{q}\|} - \frac{\dot{q}_k\,(\dot{q}_j\,\ddot{q}_j)}{\|\dot{q}\|^3} = \frac{\ddot{q}_k}{\|\dot{q}\|}. \tag{A2}$$

The last equation uses the fact that in the chosen parametrization the tangent vector $\dot{q}$ has constant length along the path and thus is perpendicular to $\ddot{q}$. Further,

$$\partial_k (g_i\,g_i)^{1/2} = \frac{g_j\,\partial_k g_j}{(g_i\,g_i)^{1/2}} = \frac{g_j\,\partial_k g_j}{\|g\|}. \tag{A3}$$

Putting this together results in

$$\left(\frac{\partial}{\partial q} - \frac{\mathrm{d}}{\mathrm{d}t}\,\frac{\partial}{\partial \dot{q}}\right) L(q,\dot{q}) = \tag{A4}$$
$$\|\dot{q}\|\,\partial_k \|g\| - \|g\|\,\frac{\mathrm{d}}{\mathrm{d}t}\,\dot{\partial}_k \|\dot{q}\| = \frac{\|\dot{q}\|}{\|g\|}\,g_j\,\partial_k g_j - \frac{\|g\|}{\|\dot{q}\|}\,\ddot{q}_k.$$

Using the arc-length parametrization where $\|\dot{q}\| = 1$, this finally leads to the Euler–Lagrange equation

$$\ddot{q} = \frac{1}{2}\,\frac{\nabla \|g\|^2}{\|g\|^2} = \nabla \log \|g\|. \tag{A5}$$